



ZnS-containing industrial waste: Antibacterial activity and effects of thermal treatment temperature and atmosphere on photocatalytic activity



Mirabbos Hojamberdiev ^{a,*}, Clara Piccirillo ^b, Yanfei Cai ^a, Zukhra C. Kadirova ^c, Kunio Yubuta ^d, Olim Ruzimuradov ^e

^a Department of Materials Physics, Nagoya University, Furo-cho, Chikusa-ku, Nagoya 464-8603, Japan

^b Nanotechnology Institute, National Research Council (CNR), Strada Provinciale Lecce-Monteroni, Campus Ecotekne, Lecce 73100, Italy

^c Uzbekistan-Japan Innovation Center of Youth, University Street 2B, Tashkent 100095, Uzbekistan

^d Institute for Materials Research, Tohoku University, 2-1-1 Katahira, Aoba-ku, Sendai 980-8577, Japan

^e Department of Natural and Mathematic Sciences, Turin Polytechnic University in Tashkent, Kichik Halqa Yo'li 17, Tashkent 100095, Uzbekistan

ARTICLE INFO

Article history:

Received 10 January 2019

Received in revised form

7 March 2019

Accepted 27 March 2019

Available online 30 March 2019

Keywords:

Zinc sulfide

Sphalerite

Thermal treatment

Antibacterial activity

Photocatalytic activity

ABSTRACT

ZnS-containing industrial waste (**ZnSW**) from the mining-metallurgy industry was characterized as a useful photocatalytic material for environmental remediation. The XRD results reveal that the **ZnSW** contains cubic ZnS (sphalerite) as a major phase and hexagonal ZnS (wurtzite), triclinic FeS₂ (pyrite) and hexagonal SiO₂ (quartz) as minor phases. The antibacterial activity of the **ZnSW** was tested for four bacterial strains. The antibacterial activity against *L. innocua* under UV light irradiation is comparable to that observed with *MRSA*, whereas the inactivation rate against *E. coli* reaches 99% within 2 h of UV light irradiation. The **ZnSW** is found to be less effective in the inactivation of *S. enteritidis*. The impact of thermal treatment temperature (400–1000 °C) and atmosphere (in air and NH₃) on photocatalytic activity of the **ZnSW** for photodegradation of gaseous acetaldehyde (AcH) and Bisphenol A (BPA) in aqueous solution under simulated solar light were investigated. The sample thermally treated at 500 °C in air completely mineralized AcH and BPA within 4 and 2 h of the photocatalytic reaction, respectively, due to the formation of a ZnS–ZnO heterojunction that promoted an effective charge separation. The sample thermally treated at 1000 °C in NH₃ exhibited the highest photocatalytic efficiency in complete photodegradation of AcH and BPA within 3.5 and 1.5 h of the photocatalytic reaction, respectively, because of the introduction of nitrogen and formation of midgap defect states. The present study demonstrates the importance of the thermal treatment temperature and atmosphere for improving the photocatalytic activity of ZnS-containing industrial waste for environmental remediation.

© 2019 Elsevier B.V. All rights reserved.

1. Introduction

A rapid industrial progress led to the generation and accumulation of massive industrial solid wastes with different chemical compositions negatively influencing the human health and the environment. Depending on their chemical compositions, such solid wastes can be efficaciously utilized to develop low-cost and high-performance materials for various applications, including environmental remediation [1–4]. Since the Honda-Fujishima

effect was first reported [5], semiconductor-based photocatalysis has been regarded as one of the most green and economical process for environmental remediation.

To date, an extensive research was carried out to develop efficient and stable photocatalytic materials for energy and environmental applications, including the utilization of solid wastes. Specifically, many attempts were made to find alternative uses for such solid wastes in photocatalysis. For instance, Maroufi et al. [6] successfully synthesized ZnO porous nanosheets with thickness of up to 100 nm from spent zinc-carbon batteries through a simple precipitation of [Zn₅(OH)₈(NO₃)₂(H₂O)₂] followed by calcination at 700 °C. The batteries-derived ZnO porous nanosheets exhibited a photodegradation efficiency of 100% for methylene blue under

* Corresponding author. Department of Materials Physics, Nagoya University, Furo-cho, Chikusa-ku, Nagoya 464-8603, Aichi, Japan.

E-mail address: hmirabbos@mp.pse.nagoya-u.ac.jp (M. Hojamberdiev).

UV–visible irradiation after 400 min, and the apparent kinetic constant was higher than that reported for multi-doped M-ZnO (M = Mg, Ca, Al, and Fe) nanoparticles [7]. Sujaridworakun and Natrchalayuth [8] used the waste zinc-dust from a hot-dip galvanizing plant as starting material for the synthesis of nano-sized ZnO photocatalyst powder via hydrothermal treatment and controlled the morphology and crystallite size of ZnO by changing the pH and the amount of hydroxypropyl cellulose (as a dispersant). The highest photocatalytic activity for the degradation of methylene blue was observed for the ZnO particles with small size and high dispersivity. Waste printed circuit boards (PCBs) were pretreated by supercritical water oxidation and then introduced into an electrokinetic system with nano-TiO₂ suspension as catholyte to prepare Cu₂O/TiO₂ composite photocatalyst, and 4.53 wt% Cu₂O/TiO₂ showed the higher photodegradation efficiency for methylene blue compared to commercial P25–TiO₂ [9].

A low-cost, high-performance titania-containing metallurgical slag photocatalysts (TCMSP_x, x = H₂SO₄, HNO₃, HCl) were prepared by acidolysis with different acids and hydrothermal synthesis and their photocatalytic activities were evaluated for photodegradation of 2,4-dichlorophenol. Under UV, visible and solar light irradiation, TCMSP_{H₂SO₄} showed the highest photocatalytic activity due to the improved UV–vis absorption, good crystallization, increased surface area, enhanced surface acidity induced by S doping [10]. The photocatalyst sample resulting from residual Ziegler-Natta catalyst slurry of the petrochemical industry achieved the highest percentage of the degradation of Rhodamine B under ultraviolet (67%) and visible (61%) light radiation because other components may act as dopants, enhancing the photostability [11]. Babar et al. [12] reported a sustainable strategy to transform waste iron rust into Fe₂O₃ nanoparticles for the synthesis of magnetically separable g-C₃N₄-Fe₂O₃ composite photocatalyst that exhibited superior photocatalytic activity for degradation of methyl orange and textile effluent.

Silicon carbide was recovered from photovoltaic industry waste and showed the highest hydrogen production rate of 191.8 μmol h⁻¹·g⁻¹ due to efficient charge transfer between 3C–SiC and 6H–SiC [13]. Salamat et al. [14] designed magnetic core–shell Fe₃O₄@TiO₂ from electric arc furnace dust and evaluated its photocatalytic activity on organic pollutant degradation from steel industry wastewater. Stable and reusable Fe₃O₄@TiO₂ showed 92.54% degradation removal efficiency of wastewater in five successive cycles. Waste multilayer ceramic capacitors (MLCC) are known to contain valuable elements. Niu and Xu [15] prepared Nb–Pb codoped and Pd loaded TiO₂ photocatalyst from waste MLCCs by a simple chlorination-leaching process, which exhibited higher photocatalytic H₂ production rate of 185.04 μmol g⁻¹·h⁻¹ and RhB degradation rate of 0.078 min⁻¹ in comparison to commercial TiO₂.

As a typical IIB–VIA group semiconductor photocatalyst, zinc sulfide (ZnS) has been intensively studied due to its wide bandgap, good stability, and low toxicity [16,17]. ZnS is known to transform from cubic, zinc-blende structure to hexagonal, wurzite structure during the temperature increase from room temperature to 500 °C [18]. A wide variety of methods has been applied for the synthesis of ZnS nanocrystals [19–21]. Previously, ZnS was reported to be a potential inorganic antibacterial reagent due to its stability, good antibacterial activity, and non-toxicity. As an example, mono-dispersed ZnS nanospheres showed high antibacterial activity against *E. coli* strain [22]. Also, ZnS nanomaterials exhibited excellent photocatalytic activity for the photodegradation of organic pollutants, such as dyes, p-nitrophenol, and halogenated benzene derivatives in wastewater [17,23–25]. Recently, we utilized ZnS-containing waste from the mining-metallurgy industry as a starting material for the synthesis of trigonal ZnIn₂S₄ layered crystals by a flux method using various binary fluxes and found that ZnIn₂S₄

crystals grown using NaCl:InCl₃ and CaCl₂:InCl₃ fluxes positively impacted the photocatalytic activity and exhibited photocatalytic H₂ evolution rates of 188 and 232 μmol h⁻¹, respectively, because of the efficient separation and transfer of photogenerated charge carriers [26].

In this study, the ZnS-containing industrial waste (**ZnSW**) from the mining-metallurgy industry was directly used as a low-cost photocatalytic material. The antibacterial activity and the impacts of thermal treatment temperature (400–1000 °C) and atmosphere (air and NH₃) on photocatalytic activity of **ZnSW** were investigated. The mechanisms for the antibacterial and photocatalytic activities of the **ZnSW** samples are also discussed.

2. Experimental

2.1. Preparation

ZnS-containing industrial waste (**ZnSW**) generated during zinc smelting process was obtained from Almalyk Mining and Metallurgical Complex, Uzbekistan and thermally treated in air in a muffle furnace and under an NH₃ flow (100 mL min⁻¹) in a horizontal tube furnace in the temperature range of 400–1000 °C for 1 h.

2.2. Characterization

The X-ray diffraction (XRD) patterns were acquired with a MiniflexII (Rigaku) diffractometer using Cu K α radiation ($\lambda = 0.15418$ nm) in the 2θ scan range of 10–80° and compared with entries from the ICDD-PDF-2 powder pattern database. The particle morphologies and sizes of the as-received and thermally treated samples were examined using a JSM-7600F field-emission-type scanning electron microscope (SEM, JEOL). The chemical composition of the samples was determined by energy dispersive X-ray spectroscopy (EDS) attached to the SEM. The crystallinity of the as-received and thermally treated **ZnSW** samples in air and NH₃ at 1000 °C for 1 h was analyzed by transmission electron microscopy (TEM, EM-002B, TOPCON) at an accelerating voltage of 200 kV. The ultraviolet–visible (UV–vis) diffuse reflectance spectra were recorded on a UV-3600 UV–vis–NIR spectrophotometer (Shimadzu) equipped with an integrating sphere, and BaSO₄ was used as a reference. The optical absorption spectra were converted from the UV–vis diffuse reflectance spectra using the Kubelka–Munk function: $F(R) = (1 - R)^2/2R = k/s$, where R is the absolute reflectance of the sampled layer, k is the molar absorption coefficient, and s is the scattering coefficient. The surface chemical composition and states of elements were analyzed by X-ray photoelectron spectroscopy (JPS-9010MC, JEOL) using non-monochromatic Mg K α radiation (1253.6 eV). The XPS profiles were fitted using a Gaussian–Lorentzian function, and the peak positions were normalized by positioning the C 1s peak at 284.5 eV. The specific surface area (S_{BET}) of the samples was determined by the Brunauer–Emmett–Teller (BET) method from the linear portion of the nitrogen gas adsorption isotherms measured at –196 °C using an Autosorb-1A (Quantachrome Instruments) after degassing the sample at 120 °C for 12 h. The thermal behavior of the **ZnSW** was studied by simultaneous thermogravimetry and differential thermal analysis (TG-DTA, Thermo plus EVO2, Rigaku) by heating 20 mg of sample from room temperature up to 1000 °C at a heating rate of 10 °C·min⁻¹ under synthetic air flow.

2.3. Antibacterial activity tests

The antibacterial activity of the as-received samples was tested on four bacterial strains: two Gram-positive (*Methicillin resistant*

Staphylococcus aureus, MRSA, ATCC 29213 and *Listeria innocua*, *L. innocua*, 11288 NCTC) and two Gram-negative (*Escherichia coli*, *E. Coli*, NCTC 9001 and *Salmonella enteritidis*, *S. enteritidis*, ATCC 3076). The fresh cultures of microorganisms were prepared by growing them in Mueller Hinton Agar at 37 °C for 24 h. The liquid cultures were successively prepared in isotonic saline solution (NaCl), with an approximate concentration of 10^{+8} CFU mL⁻¹. A weighted amount of sterile sample powder (5 mg) was placed into a sterile Petri dish (∅ 5 cm), and 4.5 mL of saline solution and 500 μL of bacterial inoculum were introduced into the Petri dish – the concentration of the powder being 1 mg mL⁻¹. The closed Petri dishes were gently shaken at 80 rpm during the tests. The experiments were performed by irradiating Petri dishes with UV light (XX-15 BLB UVP lamp), $\lambda = 365$ nm, intensity of 0.08 mW cm⁻² [27,28]. The additional experiments were also carried out with Petri dishes containing just the bacterial solutions in the dark and under UV light irradiation in the absence of the as-received and thermally treated **ZnSW** samples. At regular time intervals, aliquots of solution (50 μL) were taken from Petri dishes and diluted in isotonic NaCl solution. The diluted solutions were then placed in Petri dishes containing agar and incubated at 37 °C for 24–48 h. After the incubation, the bacterial colonies were counted. Each experiment was performed at least three times, and an average value of the bacterial counts was obtained, with the corresponding standard deviation.

2.4. Photocatalytic activity tests

Acetaldehyde (AcH), which is a typical indoor air pollutant, and Bisphenol A (BPA), which is a colorless endocrine disruptor, were selected as probe molecules to evaluate the photocatalytic activities of the as-received and thermally treated **ZnSW** samples under UV light irradiation.

Photodegradation of AcH. The photodegradation of AcH was conducted in a batch-type reactor at room temperature (25 °C). The powder sample (50 mg) was placed in a 500 mL reaction vessel made of Pyrex[®] glass, and the lid, inlet, and outlet were firmly closed. Pure air (Taiyo Nippon Sanso Corp.) was blown through the reaction vessel at room temperature to remove any air contaminants. Then, a certain amount of AcH was introduced into the reaction vessel using a 2 mL Pressure-Lok[®] glass syringe until the concentration of AcH reached about 250 ppm. After reaching the adsorption-desorption equilibrium in the dark for 12 h, the reaction vessel was placed under simulated solar light using a 300 W Xe lamp (AM1.5G filter; 18.5 mW cm⁻²). The decrease in the AcH concentration and the increase in the CO₂ concentration were monitored during the photocatalytic reaction using a GC-2014 gas chromatograph (Shimadzu), equipped with a 2 m Porapak-Q column, methanizer, and a flame ionization detector. N₂ was used as the carrier gas.

Photodegradation of BPA. The photodegradation of BPA was conducted at room temperature using a water circulating cooling system. 50 mg of powder sample was placed in a quartz test tube containing 50 mL of BPA aqueous solution with the concentration of 10 mg L⁻¹. Prior to simulated solar light irradiation (300 W Xe lamp, AM1.5G filter; 18.5 mW cm⁻²), the suspension was continuously stirred in the dark for 30 min to ensure the adsorption-desorption equilibrium. A certain amount of H₂O₂ solution was immediately introduced into the solution upon turning on the light. During the photodegradation process, approximately 2 mL of the suspension was taken out from the reactor at a predetermined time interval for subsequent analysis of BPA concentration by using a U-3010 UV–vis spectrophotometer (Hitachi).

3. Results and discussion

3.1. Characterization of ZnS-containing industrial waste

The identification of the crystalline phases present in the **ZnSW** was performed by X-ray diffraction analysis, and the XRD pattern is shown in Fig. 1a along with entry from the ICDD-PDF-2 powder pattern database for sphalerite. As shown, the most dominant diffraction peaks observed at $2\theta = 28.5, 33.0, 47.7, 56.3, 59.1,$ and 69.4° can be indexed to the (111), (200), (220), (311), (222), and (400) crystallographic planes of cubic ZnS (sphalerite) with space group *F*-43 *m* (ICDD PDF# 77–2100). The diffraction peaks noted at $2\theta = 26.6, 28.5, 30.4, 47.7,$ and 56.3° correspond to the (100), (008), (104), (110), and (118) crystallographic planes of hexagonal ZnS (wurtzite) with space group *P*6₃*mc* (ICDD PDF# 39–1363). The diffraction peaks marked at $2\theta = 28.5, 33.0, 37.1, 40.7, 47.4, 56.3,$ and 59.1° correspond to the (1–11), (002), (021), (–1–12), (–202), (113), and (2–22) crystallographic planes of triclinic FeS₂ (pyrite) (ICDD PDF# 71–1680). It should be noted that some diffraction peaks of cubic ZnS, hexagonal ZnS, and FeS₂ are overlapped, and other diffraction peaks with very low intensity were also noticed but could not be identified. The diffraction peaks observed at 20.8, 26.6, and 58.9° are attributed to the (100), (011), (211) crystallographic planes of hexagonal SiO₂ (quartz) with space group *P*3₁21 (ICDD PDF#79-1906). It can be deduced that the **ZnSW** contains cubic ZnS (sphalerite) as a dominant phase, and hexagonal ZnS, FeS₂, and SiO₂ as minor phases. The SEM image in Fig. 1b shows the particle morphology of the **ZnSW**. As shown, large plate-like and small irregular particles aggregated to form larger bulky chunks.

The thermal behavior of the **ZnSW** was investigated by TG-DTA analysis in the temperature range from room temperature up to 1000 °C in a synthetic air atmosphere, and the obtained TG-DTA curves are plotted in Fig. 1c. The first insignificant endothermic peak at about 110 °C is observed probably due to the evaporation of physically adsorbed water and melting of sulfur. An exothermic peak at about 468 °C indicates the beginning of the oxidation process of ZnS and FeS₂. Along with a major weight gain, a sharp exothermic peak at about 630 °C appears, evidencing the phase transition from ZnS and FeS₂ to ZnO and Fe₃O₄ by the influence of atmospheric oxygen [29]. The second endothermic peak noted at 815 °C is presumably attributed to the Zn₂SiO₄ phase. It should be noted that the endothermic peak confirming the formation of ZnFe₂O₄ cannot be observed in the DTA curve due to its overlapping with intense exothermic peak noted at 630 °C.

Fig. 1d shows the UV–vis diffuse reflectance spectrum of the **ZnSW**. Apparently, an optical absorption edge of the **ZnSW** is found to be at about 400 nm, corresponding to the optical band gap energy of 3.1 eV, exhibiting no absorption in the visible light region. The estimated band gap value of the **ZnSW** is much lower than that of cubic zinc blende (3.72 eV) and hexagonal wurtzite (3.77 eV) [30]. Such decrease in the band gap value is mainly associated with defects, local bond distortion, intrinsic surface states and interfaces, yielding localized electronic levels within the forbidden band gap, and the presence of minor impurities and other phases [31]. As shown, the powder color of the **ZnSW** is gray, confirming that the ZnS exists in the form of sphalerite since the wurtzite form of ZnS normally has a white or yellowish-white color.

3.2. Antibacterial activity of ZnS-containing industrial waste

Fig. 2 shows the antibacterial activity of the **ZnSW** for both Gram-positive and Gram-negative strains. Considering the Gram-positive strains, MRSA and *L. innocua*, it is clear that the sample

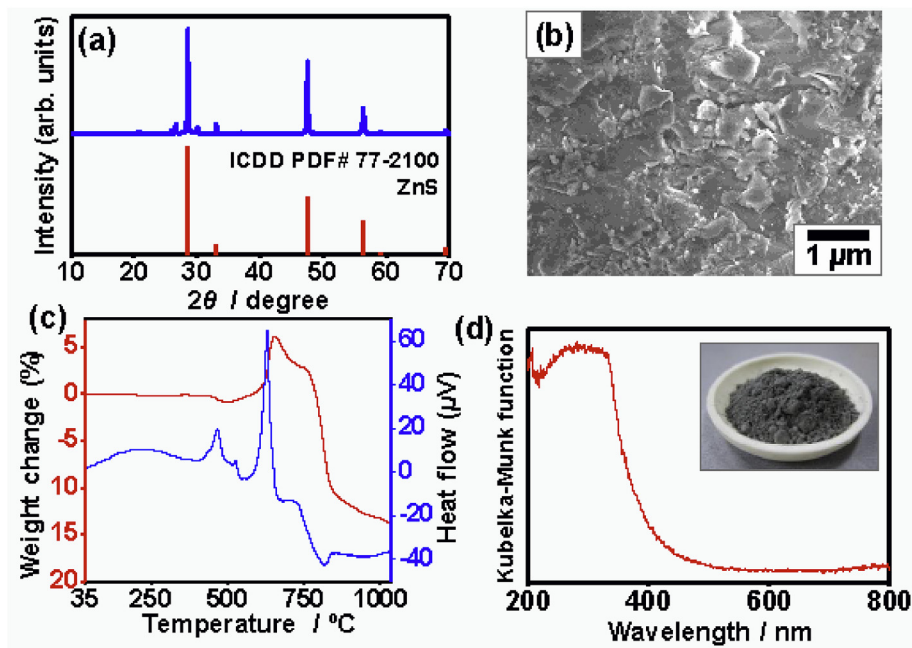


Fig. 1. (a) XRD pattern, (b) SEM image, (c) TG-DTA curves, and (c) UV-vis diffuse reflectance spectrum of ZnS-containing industrial waste.

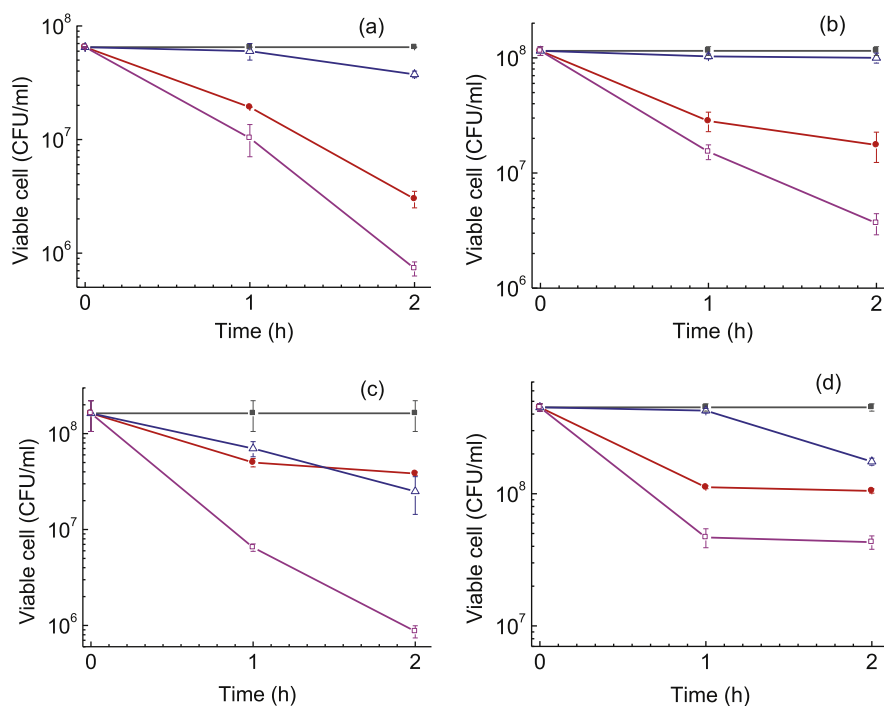


Fig. 2. Antibacterial activity of ZnS-containing industrial waste for (a) *MRSA*, (b) *L. innocua*, (c) *E. coli*, and (d) *S. enteritidis*. Keys: ■ - control test in the dark, Δ - control test under UV light, ● - sample test in the dark, □ - sample test under UV light.

shows a significant antibacterial activity towards both microorganisms. With *MRSA* (Fig. 2a), in fact, after a two-hour irradiation time the number of the bacterial population decreased of two orders of magnitude, corresponding to the inactivation rate of 99%. Interestingly, the sample showed some antibacterial activity also in the dark as a decrease in the number of the bacterial population of more than one order of magnitude was observed. This indicates that the **ZnSW** itself has an intrinsic antibacterial nature that is

enhanced by UV light irradiation. The antibacterial activity against *L. innocua* under UV light irradiation is comparable to that observed with *MRSA* (Fig. 2b). However, for the sample in the dark, a lower antibacterial activity was noted as a decrease in the number of active bacterial colonies is of only about one order of magnitude.

The **ZnSW** showed antibacterial activity also towards Gram-negative strains. The antibacterial activity against *E. coli* is shown in Fig. 2c. Evidently, a significant reduction in the viable cells was

observed after 1 h of UV light irradiation, which is more than one order of magnitude, corresponding to the inactivation rate of 90%. For an irradiation period of 2 h, the number of the bacterial population decreased by more than two orders of magnitude, corresponding to the inactivation rate of 99%. In the dark, the **ZnSW** showed no antibacterial activity, indicating the higher resistance of this strain. The **ZnSW** was found to be less effective in the inactivation of *S. enteritidis* (Fig. 2d). This is consistent with previous works confirming that this strain is more resistant to photocatalytic degradation than *E. coli* [32,33]. In fact, although a decrease in the number of the bacterial population was observed, this was of only about one order of magnitude even under UV light irradiation. Moreover, no significant difference was observed between the viable cell counts and different contact times (1 and 2 h). With respect to this strain, it can be concluded that the **ZnSW** does not behave as an effective antibacterial photocatalyst.

Previously, the antibacterial activity of ZnS was investigated, and a contradictory data was reported. For instance, Kalpana et al. [34] reported that the ZnS nanoparticles were more effective towards *E. coli* than *MRSA*, whereas the higher antibacterial activity towards the Gram-positive strain of the ZnS nanoparticles was obtained by He et al. [35]. Such difference was also obtained for other photocatalysts. As a well-known photocatalyst, TiO_2 also exhibited higher antibacterial activity towards either Gram-negative [36] or Gram-positive strains [33]. It is believed that the photocatalysts prepared with different morphologies can have different reaction pathways to generate reactive oxygen species (ROS), resulting in different antibacterial activity. Several studies reported antibacterial activity of ZnS towards *E. coli* [22,37]. To the best of our knowledge, this is the first study reporting on antibacterial activity of ZnS towards *L. innocua* or *S. enteritidis*, and the **ZnSW** can potentially be used to inactivate some bacterial strains, including *L. innocua*. As stated above, the **ZnSW** was less effective towards *S. enteritidis*.

3.3. Characterization of the thermally treated samples

Fig. 3a shows the XRD patterns of the **ZnSW** samples thermally treated in air at different temperatures ranging from 400 to 1000 °C for 1 h. As shown, cubic ZnS with space group $F-43m$ and unit cell parameters of $a = b = c = 5.411 \text{ \AA}$ and $\alpha = \beta = \gamma = 90^\circ$ (ICDD PDF# 65–1691) was identified as the main crystalline phase along with minor impurity phases: hexagonal SiO_2 (ICDD PDF# 65–0466) and triclinic FeS_2 (ICDD PDF# 65–1211) in the sample thermally treated at 400 °C. The XRD pattern of the sample thermally treated at 400 °C resembles the XRD pattern of the as-received sample, suggesting that no significant change was observed at temperatures up to 400 °C. In contrast, small diffraction peaks corresponding to hexagonal ZnO (ICDD PDF# 65–3411) were detected in addition to that of ZnS, indicating the initiation of the oxidation process of ZnS at 500 °C. At 600 °C, the diffraction peaks belonging to hexagonal ZnO became intense, and no diffraction peaks of cubic ZnS were observed, evidencing the completion of the phase transition from cubic ZnS to hexagonal ZnO [38]. Also, small diffraction peaks of cubic ZnFe_2O_4 (ICDD PDF# 65–3111) were noticed, and the formation of cubic ZnFe_2O_4 phase possibly followed the reaction steps [39,40]: (i) upon completion of the oxidation of ZnS, Fe^{2+} in FeS_2 was oxidized to Fe^{3+} and (ii) Fe^{3+} was reacted with ZnO to form ZnFe_2O_4 .

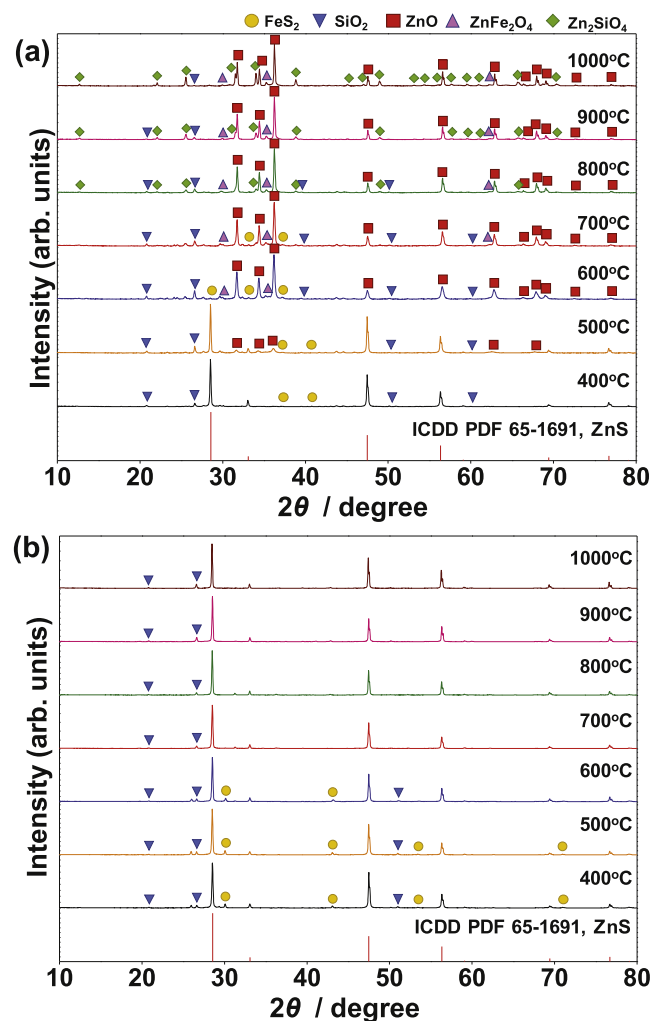
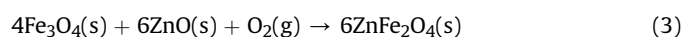
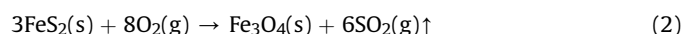
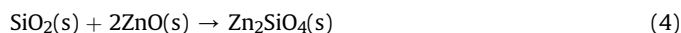


Fig. 3. XRD patterns of ZnS-containing industrial waste thermally treated at different temperatures ranging from 400 to 1000 °C in air (a) and NH_3 (b).

By increasing the temperature up to 800 °C, the FeS_2 phase completely disappeared leaving the cubic ZnFe_2O_4 phase as a still impurity phase to the main hexagonal ZnO phase. In addition, rhombohedral Zn_2SiO_4 phase (ICDD PDF# 37–1485) was formed as another impurity phase to the main hexagonal ZnO phase because of the following reaction:



Further increase in the temperature up to 1000 °C, the diffraction peaks with lower intensity of hexagonal SiO_2 were observed, and the intensity of the diffraction peaks of rhombohedral Zn_2SiO_4 became stronger [41].

Next, we studied the impact of thermal treatment in NH_3 on the **ZnSW** at different temperatures ranging from 400 to 1000 °C for 1 h, and the XRD patterns are shown in Fig. 3b. As shown, the most intense diffraction peaks in the XRD patterns can be indexed to cubic ZnS (ICDD PDF# 65–1691) as the main phase along with hexagonal SiO_2 (ICDD PDF# 65–0466) and triclinic FeS_2 (ICDD PDF# 65–1211) as the minor phases. With increasing the temperature, the diffraction peaks belonging to FeS_2 vanished gradually, and cubic ZnS and hexagonal SiO_2 remained as stable phases even at 1000 °C. In comparison with the sample thermally treated in air, the **ZnSW** thermally treated in NH_3 underwent no change in phase

transition. It can be concluded that the **ZnSW** can be converted into hexagonal ZnO as the main phase accompanied by minor phases (hexagonal SiO₂, cubic ZnFe₂O₄, and rhombohedral Zn₂SiO₄) in the temperature range of 400–1000 °C in air. Unlike in air, no phase transition in the **ZnSW** was noted during thermal treatment in NH₃.

The temperature-dependent morphological evaluation of the **ZnSW** in air and NH₃ was investigated, and the SEM results are represented in Fig. 4. As shown in Fig. 4(A) a and b, the morphologies of the samples thermally treated at 400 and 500 °C in air are mainly dominated by plate-like particles of ZnS with a rough surface. Compared with the morphology of the as-received sample, the nanocrystals of ZnO were gradually formed and grown on the surface of the samples, indicating the beginning of the oxidation process from the surface of ZnS plate-like structures. At 600 °C, the nanocrystals of ZnO were grown to platelets that eventually covered the surface, and the grown platelets were further elongated along the c-axis to form rods at 700 °C (Fig. 4(A) c and d). In the temperature range from 700 to 800 °C, the formed ZnO rods became more homogenous in size and dense (Fig. 4A e). A further increase in the temperature up to 1000 °C led to the transformation of the formed rods into irregularly shaped large grains with an average size of 430 nm (Fig. 4(A) f and g). Because when the interface or boundaries are faceted, abnormal grain growth can take place due to the relatively low energy barrier for growth [42]. Also, the resistance of solid-state diffusion is significantly reduced at higher temperature, influencing the formation of crystal [43]. Fig. 4B presents the SEM images of the **ZnSW** samples thermally treated in NH₃ at different temperatures. With increasing the thermal treatment temperature from 400 °C to 1000 °C, no significant change in morphology of ZnS structures was noticed except the rough surface became smoother, and the number of small particles on the surface decreased (Fig. 4(B) a-g).

The chemical compositions of the as-received and thermally treated **ZnSW** samples at 1000 °C in air and NH₃ were analyzed by energy-dispersive X-ray spectroscopy (EDS), and their EDS element mapping images and EDS spectra are shown in Fig. 5. In Fig. 5a, the EDS spectrum of the as-received sample confirms the presence of zinc (50.48 at%) and sulfur (47.90 at%) as major constituents, and iron (0.13 at%), silicon (0.94 at%), and potassium (0.55 at%) were also detected as a minor components. This implies that there are some minor crystalline phases in addition to the main sphalerite phase. The copper signal in the EDS spectrum comes from the sample holder. As shown in Fig. 5a and c, the Zn and S elements are homogeneously distributed in the as-received and thermally treated **ZnSW** samples in NH₃ despite the presence of oxygen traces stemming from SiO₂. Fig. 5b shows the homogenous distribution of Zn and O in the sample thermally treated at 1000 °C in air, and no traces of S are detected in the EDS spectrum, revealing the complete oxidation of ZnS.

The TEM and HRTEM images and corresponding SAED patterns of the as-received and thermally treated **ZnSW** samples at 1000 °C in air and NH₃ are represented in Fig. 6. In Fig. 6a, b and c, the bright-field TEM images show that the as-received and thermally treated in NH₃ samples have a plate-like morphology with clear edges and the ZnO crystals have irregular shape and size, respectively. The HRTEM images clearly indicate high crystallinity of the ZnS plate-like structures and irregular ZnO crystals. The SAED patterns of the as-received and thermally treated in NH₃ samples, obtained with the incident beam along the [111] and [112] zone axes, are highly ordered, confirming the single-crystalline nature of the ZnS plate-like structures. In the SAED patterns, the regular diffraction spots are consistent with the (20-2) and (2-20) and the (2-20) and (-1-11) crystallographic planes of cubic ZnS, respectively. In contrast, the SAED pattern of the sample thermally treated

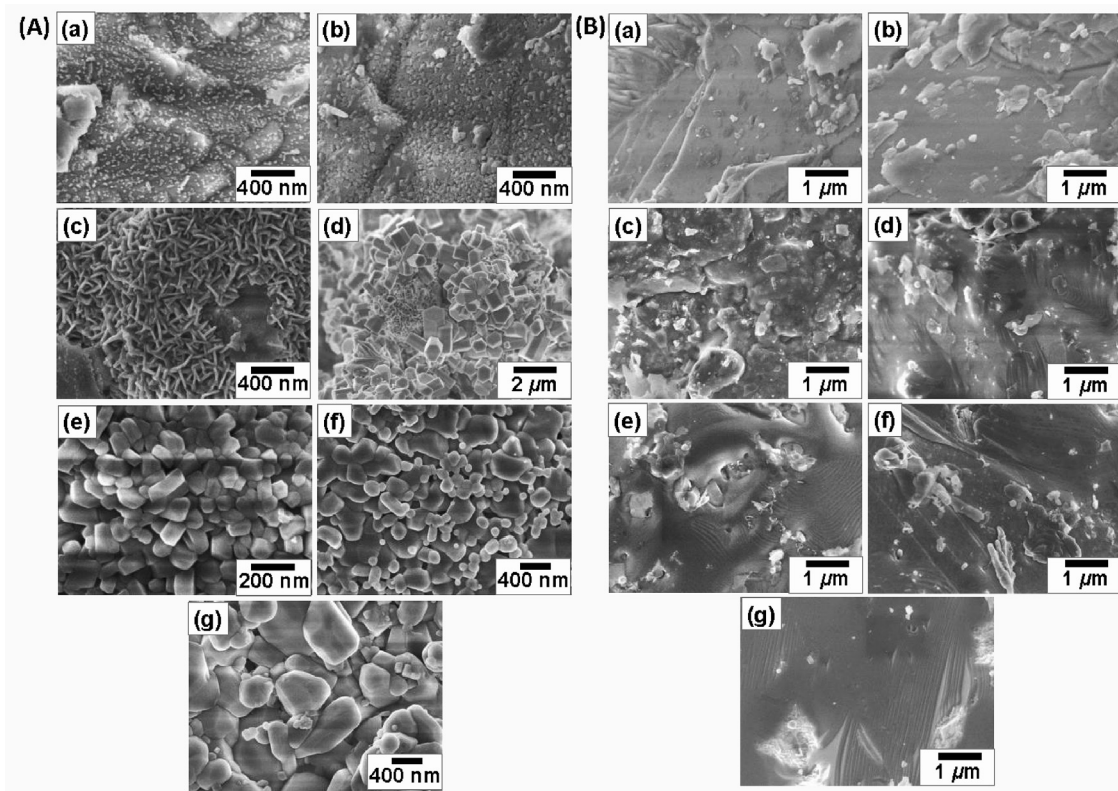


Fig. 4. SEM images of ZnS-containing industrial waste thermally treated at different temperatures in air (A) and NH₃ (B): (a) 400, (b) 500, (c) 600, (d) 700, (e) 800, (f) 900, and (g) 1000 °C.

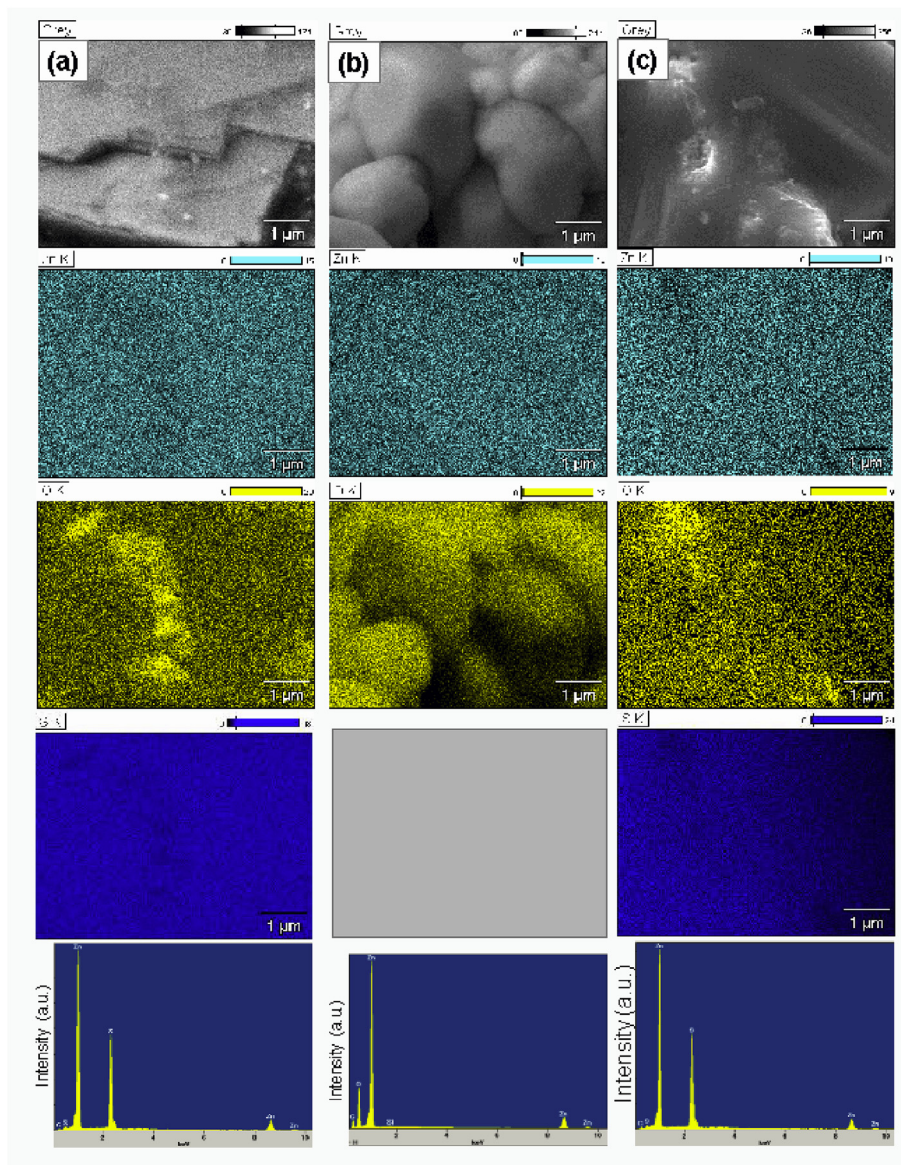


Fig. 5. EDS element mapping images and EDS spectra of the as-received (a) and thermally treated ZnS-containing industrial waste at 1000 °C in air (b) and NH₃ (c).

in air represents a set of rings instead of regular diffraction spots due to the randomly oriented crystals, confirming the polycrystalline nature of ZnO converted from ZnS.

The X-ray photoelectron spectroscopy (XPS) measurements were carried out to analyze the chemical states of elements present on the surface of the as-received and thermally treated **ZnSW** samples at 1000 °C in air and NH₃, and the Zn 2p, S 2p, O 1s, and N 1s high-resolution XPS spectra are shown in Fig. 7A. For the as-received **ZnSW** sample, the binding energies of the Zn 2p_{3/2} and Zn 2p_{1/2} peaks in ZnS are about 1021.6 and 1044.8 eV, respectively. The binding energies of the Zn 2p_{3/2} and Zn 2p_{1/2} peaks shifted from 1021.6 to 1044.8 eV to 1023.1 and 1046.3 eV and 1019.8 and 1043.0 eV for the **ZnSW** sample thermally treated at 1000 °C in air and NH₃, respectively. Such shifts in the binding energies of the Zn 2p_{3/2} and Zn 2p_{1/2} peaks are attributed to the formation of the largely ionic Zn²⁺–O²⁻ bonding and sulfur vacancy, respectively. Generally, the S 2p spectra can be deconvoluted into two peaks corresponding to the S 2p_{1/2} and S 2p_{3/2} spin-orbit doublets related to the S²⁻ oxidation state. However, the main peak noted at

161.3 eV for the as-received sample shifted to 163.0 eV for the sample thermally treated in NH₃ due to the formation of the S–Zn–N linkage [44,45]. The O 1s peak clearly observed for the sample thermally treated in air can be deconvoluted into two peaks at 530.5 and 532.0 eV assignable to the lattice oxygen in ZnO and surface-adsorbed oxygen species, respectively. The O 1s peak with low intensity was also noticed in the as-received and thermally treated in NH₃ samples due to the presence of the surface-adsorbed oxygen species. The N 1s peak noted at 399.3 eV for the sample thermally treated in NH₃ is attributed to the N–Zn bond, indicating that nitrogen was successfully doped in ZnS.

The N₂ adsorption-desorption isotherms of the as-received and thermally treated **ZnSW** samples at 1000 °C in air and NH₃ are shown in Fig. 7B. According to the IUPAC classification [46], the N₂ adsorption-desorption isotherms are type II that describes the physisorption on nonporous or macroporous adsorbents. The completion of a monolayer coverage can be noted at below 0.25 cm³ (STP) g⁻¹, and the multilayer adsorption further increases with increasing the relative pressure up to 1. A narrow hysteresis

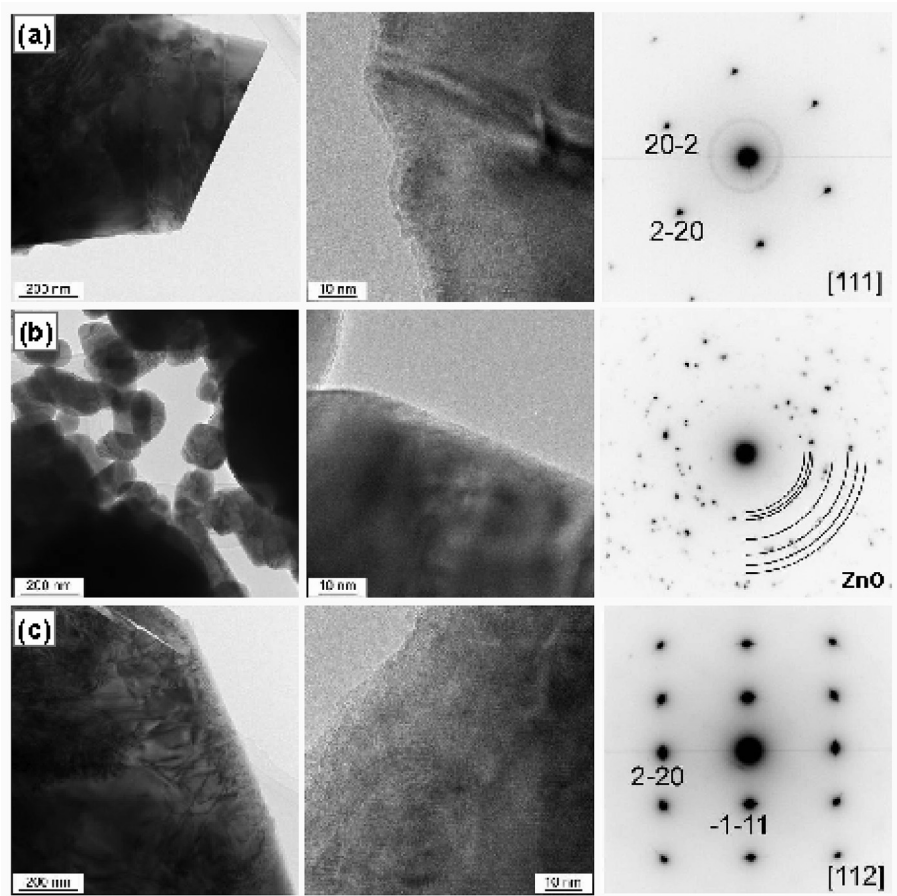


Fig. 6. TEM (left) and HR-TEM (middle) images and SAED (left) patterns of the as-received (a) and thermally treated ZnS-containing industrial waste at 1000 °C in air (b) and NH_3 (c).

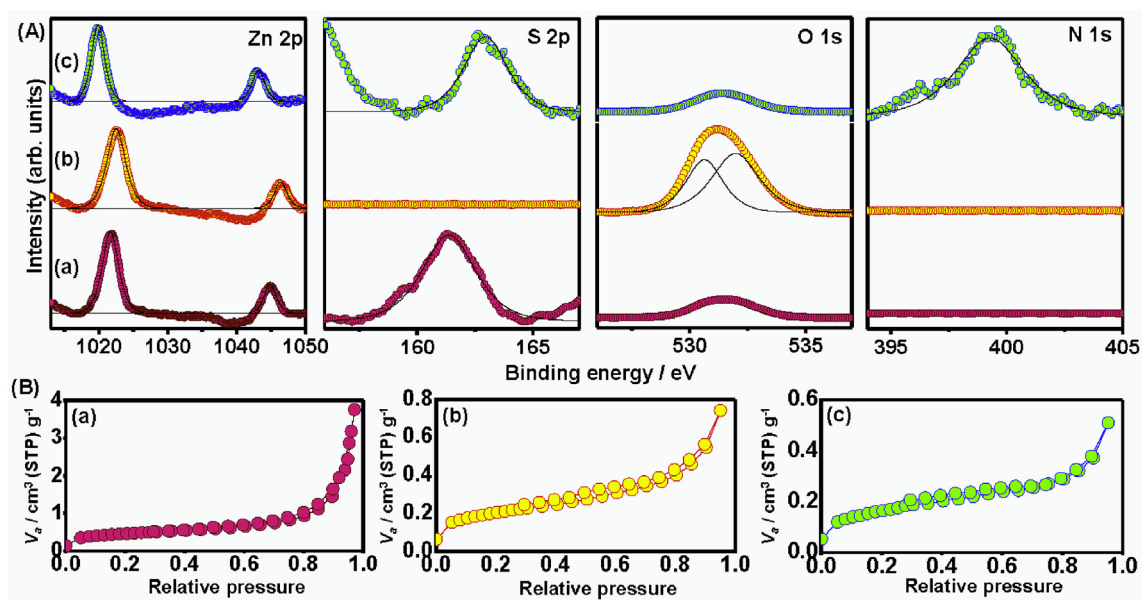


Fig. 7. (A) Zn 2p, S 2p, O 1s, and N 1s high-resolution XPS spectra and (B) N_2 adsorption-desorption isotherms of the as-received (a) and thermally treated ZnS-containing industrial waste at 1000 °C in air (b) and NH_3 (c).

loop resembles type H3, which is given by non-rigid aggregates of plate-like particles. The estimated specific surface areas of the as-received and thermally treated ZnSW samples at 1000 °C in air

and NH_3 are 1.63, 0.72, and 0.58 $\text{m}^2 \text{g}^{-1}$, respectively.

The UV–vis diffuse reflectance spectra of the ZnSW samples thermally treated at different temperatures in air and NH_3 are

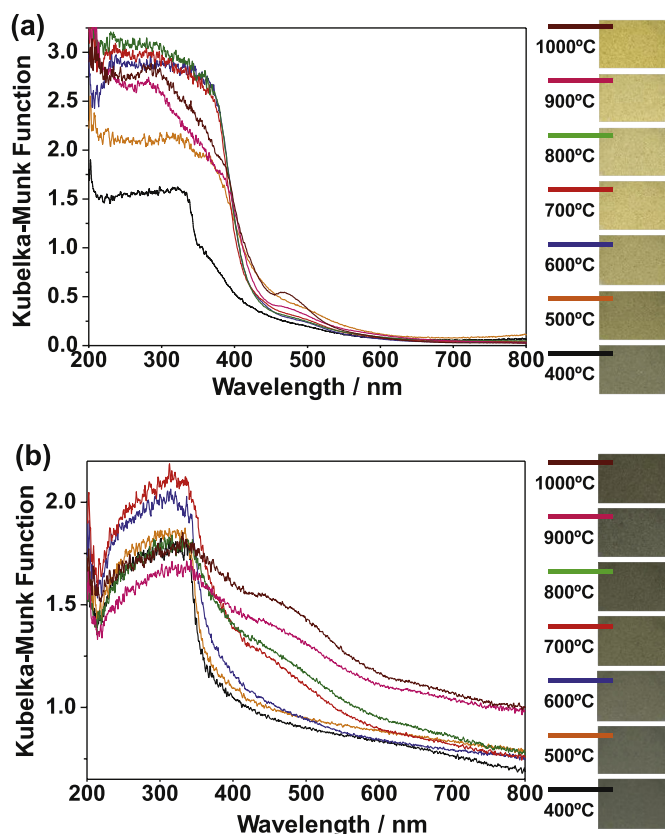


Fig. 8. UV–vis diffuse reflectance spectra of ZnS-containing industrial waste thermally treated at different temperatures ranging from 400 to 1000 °C in air (a) and NH_3 (b).

shown in Fig. 8a and b, respectively. In Fig. 8a, an absorption edge was observed at approximately 400 nm for the sample thermally treated in air at 400 °C due to the intrinsic band gap absorption of ZnS, and its corresponding band gap energy is estimated to be about 3.1 eV. When the samples were thermally treated at over 500 °C in air, their absorption edges were shifted towards longer wavelengths (about 550 nm) because of the intrinsic band gap absorption of ZnO formed from the oxidation of ZnS [47]. Presumably, an additional absorption peak (as a shoulder) started at approximately 525 nm for the sample thermally treated at 1000 °C in air is ascribed to the luminescence of Zn_2SiO_4 [48]. Unlike the UV–vis diffuse reflectance spectra of the samples thermally treated in air, the UV–vis diffuse reflectance spectra of the samples thermally treated in NH_3 exhibited an increasing absorption in the visible light region in addition to the intrinsic band gap absorption of ZnS in UV light region (Fig. 8b). With increasing the thermal treatment temperature from 400 to 1000 °C, the intensity of visible light absorption monotonically increased due to the incorporation of nitrogen into and formation of defects in the lattice of ZnS [44]. As shown in Fig. 8a, the powder color of the ZnSW was gradually altered from gray to light yellow with increasing the thermal temperature in air due to the conversion of ZnS and FeS_2 to ZnO and Fe_3O_4 and the formation of ZnFe_2O_4 . In contrast, the gray color of the ZnSW remained unchanged during the thermal treatment in NH_3 (Fig. 8b).

3.4. Photocatalytic activity of the thermally treated samples

The impacts of thermal treatment temperature and atmosphere on photocatalytic activity of the ZnSW were investigated for photodegradation of gaseous acetaldehyde (AcH) and Bisphenol A

(BPA) in aqueous solution under simulated solar light irradiation, and the results are compiled in Fig. 9. As shown, the initial concentrations of AcH and BPA gradually decreased for all samples due to the adsorption and photodegradation processes. The blank tests performed without photocatalyst under light irradiation and with photocatalyst in the dark showed no significant change in the concentrations of AcH and BPA, suggesting that the presence of photocatalyst and light irradiation were essential to drive the photodegradation process. Fig. 9a and c show that the sample thermally treated at 500 °C in air completely mineralized AcH and BPA within 4 and 2 h of the photocatalytic reaction, respectively. Among all the samples thermally treated in NH_3 , the sample treated at 1000 °C exhibited the highest photocatalytic efficiency in complete photodegradation of AcH and BPA within 3.5 and 1.5 h of the photocatalytic reaction, respectively (Fig. 9b and d). The experimentally obtained data were fitted well in the pseudo first-order kinetic equation $\ln(C/C_0) = -kt$, implying that the photodegradation of AcH and BPA follows the first-order kinetics. The estimated apparent rate constants (k values) of the samples are given in Table 1. Among the samples thermally treated in air, the sample thermally treated at 500 °C showed the highest k values of 0.00666 min^{-1} and 0.02290 min^{-1} for the degradation of AcH and BPA, respectively. The sample thermally treated at 1000 °C in NH_3 exhibited the highest k values of 0.00547 min^{-1} and 0.01565 min^{-1} for the degradation of AcH and BPA, respectively. The photocatalytic activities for photodegradation of AcH of the samples thermally treated at 500 °C in air and at 1000 °C in NH_3 are more than two and nearly eight times higher than that of the as-received sample, respectively. For photodegradation of BPA, the samples exhibited nearly nine and more than six times higher photocatalytic activities in comparison to the as-received sample, respectively. It is evident that the thermal treatment in air and NH_3 was necessary to improve the photocatalytic efficiency of the ZnSW for photodegradation of AcH and BPA under simulated solar light irradiation.

On the basis of the obtained results, the possible mechanisms for the improved photocatalytic activity of the ZnSW for photodegradation of AcH and BPA under simulated solar light irradiation are proposed here (Fig. 10a). Considering the effect of thermal treatment temperature in air on photocatalytic efficiency, 500 °C was found to be the most favorable due to the co-existence of ZnS and ZnO, which formed a heterostructure promoting an effective charge separation. Compared with the sample treated at 500 °C, the sample treated at 400 °C exhibited a slightly lower photocatalytic activity because of nonoptimal ratio of ZnS and ZnO in the heterostructure. Similarly, Hong and Kim [49] found that the ZnS–ZnO heterostructured photocatalyst fabricated at 500 °C under 16.9 kPa of O_2 partial pressure showed the highest hydrogen production rate of $494.8 \mu\text{mol g}^{-1} \cdot \text{h}^{-1}$, which is thirty seven times higher than that ($13.5 \mu\text{mol g}^{-1} \cdot \text{h}^{-1}$) of ZnS, due to the optimal content of the heterojunction. Under simulated solar irradiation, the photoinduced electrons can easily be transferred from the conduction band of ZnO to the conduction band of ZnS because the conduction band level of ZnS is lower than that of ZnO. Theoretically, the accumulated electrons in the conduction band of ZnS cannot generate $\text{O}_2^{\bullet-}$ from dissolved O_2 by photoreduction process because the conduction band edge potential of ZnS is positioned more positively than the standard redox potential $E_{(\text{O}_2/\text{O}_2^{\bullet-})}^0$. However, when the contact between ZnS and ZnO is formed, new energetic states are expected to be created at the interface, displacing the E_{fb} of the heterostructure towards negative potential, favoring the reduction of molecular oxygen to yield $\text{O}_2^{\bullet-}$ [50]. Meantime, the photoinduced holes in the valence band of ZnS migrate to the valence band of ZnO and are further involved in the oxidation of the adsorbed H_2O molecules to $\cdot\text{OH}$ because the valence band edge potential is located more positively than the standard redox potential

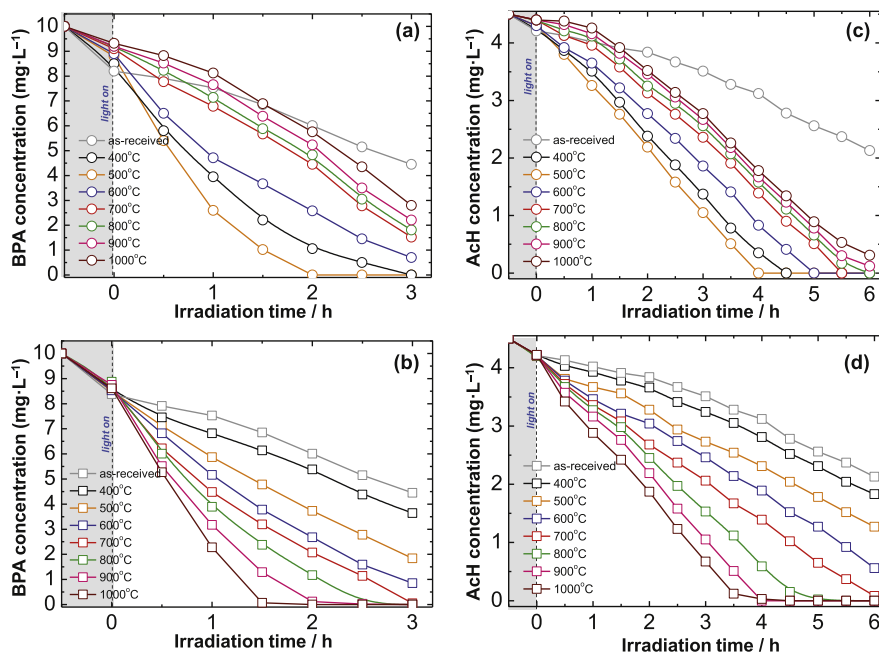


Fig. 9. Photocatalytic activities of the as-received and thermally treated ZnS-containing industrial waste at different temperatures ranging from 400 to 1000 °C in air (top) and NH₃ (bottom) for degradation of Bisphenol A in aqueous solution (a,b) and gaseous acetaldehyde (c,d).

Table 1

The estimated apparent rate constants of the samples.

Temperature, °C	k_{app}, min^{-1}			
	Acetaldehyde		Bisphenol A	
	in air	under NH ₃ atmosphere	in air	under NH ₃ atmosphere
0	0.00308	0.00261	0.00108	0.00309
400	0.00540	0.01590	0.00150	0.00434
500	0.00666	0.02290	0.00256	0.00759
600	0.00450	0.01107	0.00349	0.01119
700	0.00382	0.00664	0.00496	0.01239
800	0.00386	0.00610	0.00547	0.01565
900	0.00356	0.00523	0.00656	0.01961
1000	0.00289	0.00423	0.00846	0.02099

$E_{(-OH/H_2O)}^0$. Therefore, the photocatalytic activity of the sample thermally treated at 500 °C in air is significantly improved, and the AcH and BPA molecules were efficiently degraded through the formed $O_2^{\cdot-}$, $\cdot OH$, and direct h^+ oxidation pathway. Interestingly, the thermally treated ZnS-containing industrial waste at 400 °C in air showed much higher photocatalytic activity in comparison to the as-received sample even though the XRD patterns are quite similar, and the diffraction peaks belonging to the ZnO phase were not detected. Presumably, the ZnS-to-ZnO phase transition was initiated at 400 °C, and a small amount of the ZnO/ZnS heterojunction was formed on the surface of the ZnS particles, where the photocatalytic reaction took place. Due to the lower ZnO/ZnS ratio and lower crystallinity of the formed ZnO particles, the diffraction peaks of ZnO could not be clearly seen in the XRD pattern in Fig. 3. A further increase in the thermal treatment temperature in air led to a decrease in the photocatalytic activity due to the loss of the formed heterojunction and the increase in the crystal size of ZnO, decreasing the specific surface area and reducing the number of active sites for the adsorption of organic molecules. It is evident from Fig. 4 that increasing the thermal treatment temperature in air significantly changed the crystal morphology, leading to the loss of the faceted surfaces of ZnO, due to the crystal growth by the interfacial reaction. This additionally contributed to the decrease in

the photocatalytic activity [51]. An analogous observation was previously reported by Pardeshi and Patil [52], correlating the decreased photocatalytic degradation efficiency with the increased crystallite size. The stability of ZnSW sample thermally treated at 1000 °C in NH₃ was also evaluated by performing four successive photocatalytic experiments for the degradation of BPA. As shown in Fig. A1a in Electronic Supplementary Material, the photocatalytic activity of the ZnSW sample slightly decreased after four cycles of photocatalytic reaction, indicating that the sample has a good stability. To confirm the structural stability, the XRD patterns of ZnSW sample thermally treated at 1000 °C in NH₃ were obtained before and after the fourth cycle of the photocatalytic reaction. As shown in Fig. A1b, the XRD patterns are nearly identical, indicating a good structural stability and cyclability of the prepared ZnSW sample.

Unlike the samples thermally treated in air, the samples thermally treated in NH₃ exhibited the photocatalytic activity that increases exponentially with increasing the thermal treatment temperature. Compared with the sample thermally treated at 500 °C in air, the sample thermally treated at 1000 °C in NH₃ exhibited the highest photocatalytic activity for photodegradation of AcH and BPA under simulated solar light irradiation. Such improvement in the photocatalytic activity of the ZnSW is attributed to the extension of light absorption to the visible-light region because of the decreased band gap resulted from the introduction of nitrogen and the formation of midgap defect states. The introduction of nitrogen into ZnS creates sulfur vacancies in the anion sublattice as required by charge neutrality when N^{3-} partially replaces for S^{2-} in the structure. These sulfur vacancies act as scavengers and effectively slow down the recombination of photogenerated electrons and holes [38], improving the photocatalytic activity. It is expected that the introduction of nitrogen can further enhance the photostability of ZnS [37], prolonging the cycling time.

The molecular modeling of the interaction of the AcH and BPA + H₂O molecules with the crystallographic planes of the ZnS (111) [53] and ZnO (101) [54] was performed using a BIOVIA Material Studio - Accelrys software [2,55,56]. Fig. 10b and c show the explicit adsorption of the AcH molecules and implicit concentration

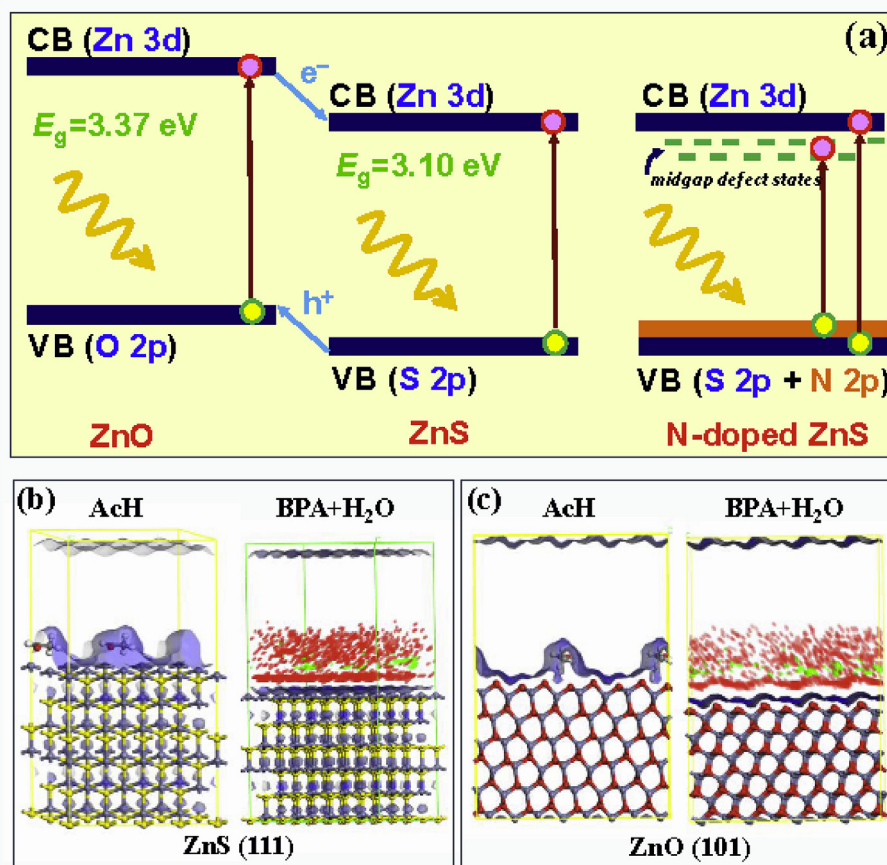


Fig. 10. (a) Schematic representation of the band structures of the samples thermally treated at 500 °C in air and 1000 °C in NH₃. Visualization of the adsorption of AcH and BPA + H₂O molecules onto the (111) surface of cubic ZnS (b) and the (101) surface of hexagonal ZnO (c). Iso-surface: Conolly surface, blue; H₂O, red; BPA, green. Atoms: oxygen, red; zinc, gray; sulfur, yellow. (For interpretation of the references to color in this figure legend, the reader is referred to the Web version of this article.)

of the field density distribution of the BPA (green) and water (red) molecules along the ZnS and ZnO surfaces. The ΔE_{ads} values of the AcH and BPA + H₂O molecules in the ZnO (in air) and ZnS (in NH₃) samples were compared:

$$\Delta E_{\text{ads}}(\text{AcH}) = E_{\text{ads}}(\text{ZnS}(111)) - E_{\text{ads}}(\text{ZnO}(101)) = 1.52 \text{ kcal mol}^{-1}.$$

$$\Delta E_{\text{ads}}(\text{BPA} + \text{H}_2\text{O}) = E_{\text{ads}}(\text{ZnS}(111)) - E_{\text{ads}}(\text{ZnO}(101)) = 10.96 \text{ kcal mol}^{-1}.$$

The ΔE_{ads} values confirm the preferential adsorption of the AcH and BPA + H₂O molecules on the ZnS surface, which is correlated with the experimentally obtained data. It should be noted that the adsorption of BPA in the presence of water molecules occurs through the hydrated layer of the crystal surface.

4. Conclusions

In summary, the ZnS-containing industrial waste (ZnSW) from the mining-metallurgy industry was characterized and its antibacterial activity against four bacterial strains was studied. The antibacterial activity against *L. innocua* under UV light irradiation was comparable to that against MRSA. The inactivation rate against *E. coli* reached 99% within 2 h of UV light irradiation, while the inactivation of *S. enteritidis* was less effective. Among the samples thermally treated in air, the sample treated at 500 °C completely mineralized AcH and BPA within 4 and 2 h of the photocatalytic reaction, respectively, due to the formation of the ZnS–ZnO

heterojunction that promoted an effective charge separation. The photocatalytic activity of the samples thermally treated in NH₃ was gradually improved with increasing the thermal treatment temperature. The sample thermally treated at 1000 °C in NH₃ exhibited the highest photocatalytic efficiency in complete photodegradation of AcH and BPA within 3.5 and 1.5 h of the photocatalytic reaction, respectively, because of the partial doping of nitrogen and the formation of midgap defect states. It was found that the thermal treatment temperature and atmosphere played a key role in improving the photocatalytic activity of the ZnS-containing industrial waste. Hence, the ZnS-containing industrial waste can be a useful, low-cost photocatalytic material after thermal treatment for environmental remediation.

Appendix A. Supplementary data

Supplementary data to this article can be found online at <https://doi.org/10.1016/j.jallcom.2019.03.368>.

References

- [1] Z.C. Kadirova, M. Hojamberdiev, L. Bo, R. Hojiyev, K. Okada, Simultaneous removal of NH₄⁺, H₂PO₄⁻ and Ni²⁺ from aqueous solution by thermally activated combinations of steel converter slag and spent alumina catalyst, *J. Water Process Eng.* 8 (2015) 151–159.
- [2] M. Hojamberdiev, S.S. Daminova, Z.C. Kadirova, K.T. Sharipov, F. Mtalo, M. Hasegawa, Ligand-immobilized spent alumina catalyst for effective removal of heavy metal ions from model contaminated water, *J. Environ. Chem. Eng.* 6 (2018) 4623–4633.
- [3] B. Czech, M. Hojamberdiev, A. Bogusz, Impact of thermal treatment of calcium silicate-rich slag on the removal of cadmium from aqueous solution, *J. Clean.*

- Prod. 200 (2018) 369–379.
- [4] M. Hojamberdiev, Y. Kameshima, A. Nakajima, K. Okada, Z. Kadirova, Preparation and sorption properties of materials from paper sludge, *J. Hazard. Mater.* 151 (2008) 710–719.
- [5] A. Fujishima, K. Honda, Electrochemical photolysis of water at a semiconductor electrode, *Nature* 238 (1972) 37–38.
- [6] S. Maroufi, R.K. Nekouei, M. Assefi, V. Sahajwalla, Waste-cleaning waste: synthesis of ZnO porous nano-sheets from batteries for dye degradation, *Environ. Sci. Pollut. Res.* 25 (2018) 28594–28600.
- [7] Z.-J. Wu, W. Huang, K.-K. Cui, Z.-F. Gao, P. Wang, Sustainable synthesis of metals-doped ZnO nanoparticles from zinc-bearing dust for photodegradation of phenol, *J. Hazard. Mater.* 278 (2014) 91–99.
- [8] P. Sujaridworakun, K. Natrchalayuth, Influence of pH and HPC concentration on the synthesis of zinc oxide photocatalyst particle from zinc-dust waste by hydrothermal treatment, *Adv. Powder Technol.* 25 (2014) 1266–1272.
- [9] F.-R. Xiu, F.-S. Zhang, Preparation of nano-Cu₂O/TiO₂ photocatalyst from waste printed circuit boards by electrokinetic process, *J. Hazard. Mater.* 172 (2009) 1458–1463.
- [10] H. Liu, T. Xia, H.K. Shon, S. Vigneswaran, Preparation of titania-containing photocatalysts from metallurgical slag waste and photodegradation of 2,4-dichlorophenol, *J. Ind. Eng. Chem.* 17 (2011) 461–467.
- [11] W.L. da Silva, M.A. Lansarin, F.C. Stedile, J.H.Z. dos Santos, The potential of chemical industrial and academic wastes as a source of supported photocatalysts, *J. Mol. Catal. A* 393 (2014) 125–133.
- [12] S. Babar, N. Gavade, H. Shinde, P. Mahajan, K.H. Lee, N. Mane, A. Deshmukh, K. Garadkar, V. Bhuse, Evolution of waste iron rust into magnetically separable g-C₃N₄-Fe₂O₃ photocatalyst: an efficient and economical waste management approach, *ACS Appl. Nano Mater.* 1 (2018) 4682–4694.
- [13] Y. Zhang, Y. Hu, H. Zeng, L. Zhong, K. Liu, H. Cao, W. Li, H. Yan, Silicon carbide recovered from photovoltaic industry waste as photocatalysts for hydrogen production, *J. Hazard. Mater.* 329 (2017) 22–29.
- [14] S. Salamat, H. Younesi, N. Bahramifar, Synthesis of magnetic core-shell Fe₃O₄@TiO₂ nanoparticles from electric arc furnace dust for photocatalytic degradation of steel mill wastewater, *RSC Adv.* 7 (2017) 19391–19405.
- [15] B. Niu, Z. Xu, *In-situ* preparation of Nb-Pb codoped and Pd loaded TiO₂ photocatalyst from waste multi-layer ceramic capacitors by a chlorination-leaching process, *Green Chem.* 21 (2019) 874–884.
- [16] S. Yanagida, K. Mizumoto, C. Pac, Semiconductor photocatalysis. Part 6. Cis-trans photoisomerization of simple alkenes induced by trapped holes at surface states, *J. Am. Chem. Soc.* 108 (1986) 647–654.
- [17] J.S. Hu, L.L. Ren, Y.G. Guo, H.P. Liang, A.M. Cao, L.J. Wan, C.L. Bai, Mass production and high photocatalytic activity of ZnS nanoporous nanoparticles, *Angew. Chem. Int. Ed.* 44 (2005) 1269–1273.
- [18] S.B. Qadri, E.F. Skelton, D. Hsu, A.D. Dinsmore, J. Yang, H.F. Gray, B.R. Ratna, Size-induced transition-temperature reduction in nanoparticles of ZnS, *Phys. Rev. B* 60 (1999) 9191.
- [19] I.U. Arachchige, S.L. Brock, Highly luminescent quantum-dot monoliths, *J. Am. Chem. Soc.* 129 (2007) 1840–1841.
- [20] N. Hebbalkar, A. Lobo, S.R. Sainkar, S.D. Pradhan, W. Vogel, J. Urban, S.K. Kulkarni, Properties of zinc sulphide nanoparticles stabilized in silica, *J. Mater. Sci.* 36 (2001) 4377–4384.
- [21] R. Kho, C.L. Torres-Martínez, R.K. Mehra, A simple colloidal synthesis for gram-quantity production of water-soluble ZnS nanocrystal powders, *J. Colloid Interface Sci.* 227 (2000) 561–566.
- [22] G. Li, J. Zhai, D. Li, X. Fang, H. Jiang, Q. Dong, E. Wang, One-pot synthesis of monodispersed ZnS nanospheres with high antibacterial activity, *J. Mater. Chem.* 20 (2010) 9215–9219.
- [23] H. Yin, Y. Wada, T. Kitamura, S. Yanagida, Photoreductive dehalogenation of halogenated benzene derivatives using ZnS or CdS nanocrystallites as photocatalysts, *Environ. Sci. Technol.* 35 (2001) 227–231.
- [24] Y. Wada, T. Kitamura, S. Yanagida, H. Yin, Photoreductive dechlorination of chlorinated benzene derivatives catalyzed by ZnS nanocrystallites, *Chem. Commun.* 0 (1998) 2683–2684.
- [25] M. Sharma, T. Jain, S. Singh, O.P. Pandey, Photocatalytic degradation of organic dyes under UV-Visible light using capped ZnS nanoparticles, *Sol. Energy* 86 (2012) 626–633.
- [26] M. Hojamberdiev, Y. Cai, J.J.M. Vequizo, M.M. Khan, R. Vargas, K. Yubuta, A. Yamakata, K. Teshima, M. Hasegawa, Binary flux-promoted formation of trigonal ZnIn₂S₄ layered crystals using ZnS-containing industrial waste and their photocatalytic performance for H₂ production, *Green Chem.* 20 (2018) 3845–3856.
- [27] C. Piccirillo, R.A. Pinto, D.M. Tobaldi, R.C. Pullar, J.A. Labrincha, M.M.E. Pintado, P.M.L. Castro, Light induced antibacterial activity and photocatalytic properties of Ag/Ag₃PO₄-based material of marine origin, *J. Photochem. Photobiol., A* 296 (2015) 40–47.
- [28] C. Piccirillo, R.C. Pullar, D.M. Tobaldi, P.M. Lima Castro, M.M. Estevez Pintado, Silver-containing calcium phosphate materials of marine origin with antibacterial activity, *Ceram. Int.* 41 (2015) 10152–10159.
- [29] T. Kryshtab, V.S. Khomchenko, J.A. Andraca-Adame, A.K. Savin, A. Kryvko, G. Juárez, R. Peña-Sierra, Luminescence and structure of ZnO–ZnS thin films prepared by oxidation of ZnS films in air and water vapor, *J. Lumin.* 129 (2009) 1677–1681.
- [30] X. Fang, T. Zhai, U.K. Gautam, L. Li, L. Wu, Y. Bando, D. Golberg, ZnS nanostructures: from synthesis to applications, *Prog. Mater. Sci.* 56 (2011) 175–287.
- [31] F.A. La Porta, J. Andrés, M.S. Li, J.R. Sambrano, J.A. Varela, E. Longo, Zinc blende versus wurtzite ZnS nanoparticles: control of the phase and optical properties by tetrabutylammonium hydroxide, *Phys. Chem. Chem. Phys.* 16 (2014) 20127–20137.
- [32] J.M.C. Robertson, P.K.J. Robertson, L.A. Lawton, A comparison of the effectiveness of TiO₂ photocatalysis and UVA photolysis for the destruction of three pathogenic micro-organisms, *J. Photochem. Photobiol., A* 175 (2005) 51–56.
- [33] H.M. Yadav, S.V. Otari, R.A. Bohara, S.S. Mali, S.H. Pawar, S.D. Delekar, Synthesis and visible light photocatalytic antibacterial activity of nickel-doped TiO₂ nanoparticles against Gram-positive and Gram-negative bacteria, *J. Photochem. Photobiol., A* 294 (2014) 130–136.
- [34] K. Kalpana, V. Selvaraj, Photodegradation and antibacterial studies of ZnS wrapped fly ash nanocomposite for multipurpose industrial applications, *RSC Adv.* 5 (2015) 47766–47777.
- [35] W. He, H. Jia, J. Cai, X. Han, Z. Zheng, W.G. Wamer, J.J. Yin, Production of Reactive Oxygen Species and electrons from photoexcited ZnO and ZnS nanoparticles: a comparative study for unravelling their distinct photocatalytic activity, *J. Phys. Chem. C* 120 (2016) 3187–3195.
- [36] D.M. Tobaldi, C. Piccirillo, N. Rozman, R.C. Pullar, M.P. Seabra, A.S. Škapinc, P.M.L. Castro, J.A. Labrincha, Effects of Cu, Zn and Cu-Zn addition on the microstructure and antibacterial and photocatalytic functional properties of Cu-Zn modified TiO₂ nano-heterostructures, *J. Photochem. Photobiol., A* 330 (2016) 44–54.
- [37] Y. Chen, Q. Ma, H. Jia, Y. Wang, Hydrothermal synthesis of ZnS microspheres with highly effective photocatalytic and antibacterial properties, *J. Mater. Sci. Mater. Electron.* 27 (2016) 10237–10244.
- [38] D. Schultze, U. Steinike, J. Kussin, U. Kretzschmar, Thermal oxidation of ZnS modifications sphalerite and wurtzite, *Cryst. Res. Technol.* 30 (1995) 553–558.
- [39] S. Heukelman, D. Groot, Fluidized bed roasting of micro-pelletized zinc concentrate: Part II—Particle entrainment and residence time, *J. S. Afr. Inst. Min. Metall.* 111 (2011) 767–772.
- [40] J.W. Graydon, D.W. Kirk, A Microscopic study of the transformation of sphalerite particles during the roasting of zinc concentrate, *Metall. Trans. B* 19 (1988) 141–146.
- [41] M. Llugar, A. Forés, J.A. Badenes, J. Calbo, M.A. Tena, G. Monrós, Colour analysis of some cobalt-based blue pigments, *J. Eur. Ceram. Soc.* 21 (2001) 1121–1130.
- [42] M.S. Kim, J.G. Fisher, S.J.L. Kang, Grain growth control and solid-state crystal growth by Li₂O/PbO addition and dislocation introduction in the PMN–35PT system, *J. Am. Ceram. Soc.* 89 (2006) 1237–1243.
- [43] G. Hu, K. Dam-Johansen, S. Wedel, Solid-state diffusion and crystal growth: two important steps for gas-solid reactions, in: Proceedings of European Congress of Chemical Engineering (ECCE-6), Copenhagen, 2007, pp. 16–20.
- [44] Y. Zhou, G. Chen, Y. Yu, Y. Feng, Y. Zheng, An efficient method to enhance the stability of sulphide semiconductor photocatalysts: a case study of N-doped ZnS, *Phys. Chem. Chem. Phys.* 17 (2015) 1870–1876.
- [45] G. Wang, B. Huang, Z. Li, Z. Lou, Z. Wang, Y. Dai, M.H. Whangbo, Synthesis and characterization of ZnS with controlled amount of S vacancies for photocatalytic H₂ production under visible light, *Sci. Rep.* 5 (2015) 8544.
- [46] M. Thommes, K. Kaneko, A.V. Neimark, J.P. Olivier, F. Rodriguez-Reinoso, J. Rouquerol, K.S.W. Sing, Physisorption of gases, with special reference to the evaluation of surface area and pore size distribution (IUPAC Technical Report), *Pure Appl. Chem.* 87 (2015) 1051–1069.
- [47] J.S. Jang, C.J. Yu, S.H. Choi, S.M. Ji, E.S. Kim, J.S. Lee, Topotactic synthesis of mesoporous ZnS and ZnO nanoplates and their photocatalytic activity, *J. Catal.* 254 (2008) 144–155.
- [48] X.D. Wang, C.J. Summers, Z.L. Wang, Mesoporous single - crystal ZnO nanowires epitaxially sheathed with Zn₂SiO₄, *Adv. Mater.* 16 (2004) 1215–1218.
- [49] E. Hong, J.H. Kim, Oxide content optimized ZnS–ZnO heterostructures via facile thermal treatment process for enhanced photocatalytic hydrogen production, *Int. J. Hydrogen Energy* 39 (2014) 9985–9993.
- [50] Y. Piña-Pérez, O. Aguilar-Martínez, P. Acevedo-Peña, C.E. Santolalla-Vargas, S. Oros-Ruiz, F. Galindo-Hernández, R. Gómez, F. Tzompantzi, Novel ZnS-ZnO composite synthesized by the solvothermal method through the partial sulfidation of ZnO for H₂ production without sacrificial agent, *Appl. Catal., B* 230 (2018) 125–134.
- [51] D. Li, H. Haneda, Morphologies of zinc oxide particles and their effects on photocatalysis, *Chemosphere* 51 (2003) 129–137.
- [52] S.K. Pardeshi, A.B. Patil, Effect of morphology and crystallite size on solar photocatalytic activity of zinc oxide synthesized by solution free mechanochemical method, *J. Mol. Catal. A* 308 (2009) 32–40.
- [53] E.A. Jumpertz, Electron-density distribution in zinc blende, *Z. Elektrochem.* 59 (1955) 419–425.
- [54] G. Aminoff, XXIV. Über Lauephotogramme und Struktur von Zinkit, *Z. Kristallogr.* 56 (1921) 495–505.
- [55] M. Hojamberdiev, Z.C. Kadirova, R.V. Gonçalves, K. Yubuta, N. Matsushita, K. Teshima, M. Hasegawa, K. Okada, Reduced graphene oxide-modified Bi₂WO₆/BiOI composite for the effective photocatalytic removal of organic pollutants and molecular modeling of adsorption, *J. Mol. Liq.* 268 (2018) 715–727.
- [56] M. Hojamberdiev, Z.C. Kadirova, Y. Makinose, G. Zhu, N. Matsushita, J. Rodríguez, S. Aldabe Bilmes, M. Hasegawa, K. Okada, Influence of BiOI content on the photocatalytic activity of Bi₂WO₆/BiOI/allopahane composites and molecular modeling studies of acetaldehyde adsorption, *J. Taiwan Inst. Chem. Eng.* 81 (2017) 258–264.